Efficient recovery of lithium from spent lithium-ion battery raffinate by Mn and Al-based adsorbents: pretreatment, adsorption mechanism, and performance comparison

In preparation for ***Separation and Purification Technology***

Data: April 18, 2024

Efficient recovery of lithium from spent lithium-ion battery raffinate by Mn and Al-based adsorbents: pretreatment, adsorption mechanism, and performance comparison

*Xifan Li [a, b], Xin Li [a, b], Guijing Chen [a, b], Hui Li [c], Yi Duan [c], Yu Sun [c], Alberto Tiraferri [d], Baicang Liu [a, b, *]*

[a] State Key Laboratory of Hydraulics and Mountain River Engineering, College of Architecture and Environment, Institute of New Energy and Low-Carbon Technology, Institute for Disaster Management and Reconstruction, Sichuan University, Chengdu, Sichuan 610207, PR China

[b] Yibin Institute of Industrial Technology, Sichuan University Yibin Park, Yibin, Sichuan 644000, PR China

[c] CCDC Safety, Environment, Quality Supervision & Testing Research Institute, Guanghan, Sichuan 618300, PR China

[d] Department of Environment, Land and Infrastructure Engineering, Politecnico di Torino, Corso Duca degli Abruzzi 24, 10129 Turin, Italy

[*]Corresponding author. Tel.: +86-28-85995998; fax: +86-28-62138325; E-mail: bcliu@scu.edu.cn; baicangliu@gmail.com (B. Liu).

Abstract:

As a strong wave of retired lithium-ion battery approaches, lithium extraction from spent lithium-ion battery raffinate (SLR) becomes increasingly critical for environmental protection and for sustainable lithium supply. To understand the factors that affect maximum recovery of lithium from SLR, the organic and inorganic components of SLR were initially determined. The organic matter content (up to 760.5 mg/L) seriously impacted the recovery rate of lithium. Therefore, SLR was managed with a series of pretreatment techniques, including coagulation, biochar aerogel adsorption, and ultrafiltration, achieving more than 84.3% removal of organic substances. $H_{1.33}Mn_{1.67}O_4$ and Li/Al layered double hydroxides adsorbents were then synthesized by solid state reaction method and hydrothermal method, respectively, granulated into spheres with a PVC skeleton, and applied to recycle lithium from pretreated SLR in a fixed bed adsorption column. The results indicated that both Mn and Al-based adsorbents exhibited rapid adsorption kinetics, reaching saturation within 2 h. The Mn-based adsorbent exhibited superior adsorption selectivity for Li^+ and higher Li^+/Na^+ separation factor (α_{Na}^{Li}) compared to Al-based adsorbent, with partition coefficients and α_{Na}^{Li} values equal to 6.62 mL/g, 8.79 for the former material, and 4.92 mL/g, 8.17 for the latter. On the other hand, the Al-based adsorbent displayed better stability with negligible Al loss, while Mn loss from the related adsorbent was less than 0.2% in every adsorption-desorption cycle. Notably, both adsorbents demonstrated excellent reusability with their adsorption capacity maintained after twenty adsorption-desorption cycles.

Key words:

Spent lithium-ion battery raffinate; Pretreatment; Lithium recycling; Mn/Al-based adsorbent; Comparative analysis.

1. Introduction

As a critical rare metal [1], lithium has extensive application in various industrial applications, chiefly, in lithium batteries [2] due to its light mass density (0.534 g/cm^3) [3], high electrode potential (–3.05 V) [4], low equivalent weight (6.94 g/Faraday) [5], and long service life. In the context of "dual carbon" objective, the market for new energy vehicles powered by lithium-ion batteries (LIB) has experienced exponential growth as a response to the scarcity of fossil fuels and climate change [6], resulting in a substantial increase in the production of lithium-ion batteries. By 2030, China's electric vehicle production is projected to reach 15 million per year [7], accounting for 45% of the global total electric vehicles based on reports from the International Energy Agency [5]. However, after a lifespan of 3 to 10 years [8], a great deal of electric vehicles will be retired, leading to a significant accumulation of spent LIBs [9,10]. The China Society of Automotive Engineers estimates that, by 2030, the amount of decommissioned power batteries will reach 3.5 million tons. However, the global lithium recycling rate from LIBs is below 1% [11]. Survey of Development Research of the State Council indicates that the standardized recovery rate of China's new energy vehicle power battery is less than 25% in 2023.

If handled improperly and if disposed as domestic waste, the heavy metals and toxic electrolytes in spent LIBs will cause environmental problems and threats to human health [12,13]. However, a large amount of valuable key metal ions, such as Li, Co, Ni, and Mn in spent LIBs have high grade and are potentially easier to recover than extraction from natural ores, which makes spent LIBs a secondary, economical source

of valuable minerals [10,14,15]. In particular, the content of Li in spent LIBs reaches up to 5 to 7 wt% [16], which is substantially higher than any other lithium resource. Therefore, recovering rare metals from spent LIBs is of great significance for mitigating environmental pollution and ensuring a sustainable supply of lithium as raw material for the manufacturing of new batteries.

Hydrometallurgy [17], pyrometallurgy [18], biometallurgy [19], and electrochemical extraction [20] have been employed in research and industrial settings for metals recovery from spent LIBs. Among these methods, hydrometallurgy combined with leaching and extraction is the most common method adopted for metal ion recycling [21]. The hydrometallurgy process requires a large volume of strong acid and water for leaching, followed by pH adjustment, typically performed by addition of NaOH, to extract Mn, Co, and Ni in sequence [22]. Spent lithium-ion battery raffinate (SLR) is the leachate of spent LIBs obtained after the extraction of Mn, Co, Ni, and Li. It contains large concentrations of Na and residual Li, and it is characterized by high values of total dissolved solids (TDS) and total organic carbon (TOC). The lithium concentration in the raffinate can reach up to 1000 mg/L, higher than that found in traditional salt lake brine, seawater, or shale gas wastewater. It is thus potentially feasible to further extract Li from the raffinate to further increase lithium supply and to alleviate environmental pollution.

Currently, most literature studies on this topic focus on lithium recycling directly from the spent LIBs or from salt lake brines, with limited attention paid to lithium recycling from RSL. Presently, methods for lithium recovery from aqueous lithium

89 resources include evaporation and precipitation [23], solvent extraction [24],
90 adsorbents adsorption [25], membrane treatment [4,26], electrochemical methods [27],
91 or a combination of the above. Among these approaches, membrane and
92 electrochemical methods are not readily applicable, due to the high TDS and TOC
93 content of RSL. Instead, adsorbents have gained widespread attention due to their
94 simplicity in preparation, low synthesis contamination, high adsorption capacity and
95 selectivity, as well as reusability and economic potential [25].

96 There are three main types of inorganic metal-based lithium ion adsorbents
97 extensively applied for lithium extraction, including layered Al-based adsorption
98 materials, Mn-based ion sieves, and Ti-based ion sieves [25,28]. The lithium adsorption
99 process of these metal-based ion sieves is mainly governed by structural memory effect
100 [28]. Ti-based ion-exchange sieves have strong Ti-O bonds, which endow them with a
101 stable framework, excellent acid endurance, and exceptional Li adsorption ability [29].
102 However, high cost thwarts the practical application of these Ti-based materials. Al-
103 based adsorbents have exhibited better potential in industrial applications, owing to
104 their technological maturity, inexpensive raw materials, simple synthesis procedure,
105 and mild preparation conditions [30]. For example, Zhong et al [31]. synthesized two-
106 dimensional hexagonal Li/Al layered double hydroxides by coprecipitation to recover
107 Li from Qarhan salt lake brine at ambient temperature, with an adsorption capacity of
108 7.27 mg/g. Sun et al. prepared Li/Al layered double hydroxides and extracted Li from
109 Qaidam salt lake brine by hybrid method of reaction-coupled separation, reaching Li
110 loss lower than 3.93% [32]. In addition, Mn-based adsorbents present excellent

adsorption performance, selectivity, regeneration properties, and low cost [33]. Compared with $H_{1.6}Mn_{1.6}O_4$ and $HMnO_2$ [34], the synthesis of $H_{1.33}Mn_{1.67}O_4$ is simpler due to lower energy requirement [35]. For instance, Tian et al. synthesized $H_{1.33}Mn_{1.67}O_4$ and recovered lithium from shale gas wastewater, reaching a Li partition coefficient higher than 1073 mL/g [36]. Both Al-based and $H_{1.33}Mn_{1.67}O_4$ adsorbents have reliable application potential for lithium recovery from SLR.

This study discusses and evaluates the technical feasibility of lithium recycling from SLR, as a novel potential source of lithium. We first investigate the characteristics of SLR and the effect of pretreatment, including coagulation, biochar adsorption, and ultrafiltration, on organic pollutant removal. Then, we discuss the synthesis of Li/Al layered double hydroxides and of $Li_{1.33}Mn_{1.67}O_4$ adsorbent precursors by one step method and solid-phase reaction method, respectively, and the granulation of the adsorbents powder into spheres aimed at lithium recycling from SLR in a fixed bed adsorption column. The adsorption kinetics, adsorption selectivity, multi-stage adsorption performance, and regeneration capability of lithium recovery from SLR by both Mn and Al-based adsorbent granules are evaluated. Adsorbents are also assessed in terms of adsorption/desorption performance during 20 cycles of utilization. The main objective is to verify the technical feasibility of lithium recovery from real SLR by pretreatment combined with adsorption, which has important repercussions on further development of lithium recycling strategies.

2. Materials and methods

2.1. Materials

AR-grade $MnCO_3$, Li_2CO_3, $AlCl_3 \cdot 6H_2O$, NaOH, and HCl and were purchased from Kelong Chemical Co., Ltd. (Chengdu, China) Polyaluminum chloride (PACl) was purchased from Liming chemical plant (Zigong, China). Polyvinyl chloride (PVC) and dimethylacetamide (DMAC) were supplied by Macklin Biochemical Co., Ltd. (Shanghai, China). The raw SLR solution was provided by Botree Recycling Technologies Co., Ltd. (Suzhou, China). All chemicals were used as received.

2.2. Synthesis of Mn and Al-based adsorbent powders precursor

The Mn-based adsorbent precursor for $Li_{1.33}Mn_{1.67}O_4$ was prepared by solid state reaction method, with synthesis processes detailed in our previous work [36]. Briefly, a proper amount of $MnCO_3$ and Li_2CO_3 powders with Li/Mn molar ratio of 1.33:1.67 were well-mixed in a ceramic mortar, then calcinated in a tube furnace at 500 ºC for 4 h under ambient air with heating rate of 3 ºC/min, followed by cooling to ambient temperature. The Al-based lithium adsorbent precursor was synthesized by a one-step method. $AlCl_3 \cdot 6H_2O$ and LiCl were dissolved in ultrapure water at an Al/Li mole ratio of 1.3:1. NaOH solution with a concentration of 5 mol/L was added dropwise to the above solution with assistance of a peristaltic pump at a rate of 3.5 mL/min while stirring at a speed of 150 r/min. The reaction temperature was 75 ºC and the terminal pH was 6-7. The obtained solid was separated from the aqueous solution by centrifugation and dried to obtain the Al-based adsorbent precursor.

2.3. Granular Mn and Al-based adsorbent preparation

Adsorbent precursor powders were granulated into spheres by anti-solvent method, as follows: 3.5 g PVC was added in 40 mL DMAC solution under magnetic stirring at

60 ºC until dissolved completely. Then, 4.0 g adsorbent precursor powder was added to this solution to form a uniform slurry. After that, the slurry was dripped by a syringe pump into ultrapure water to form granules. The obtained spheres were rinsed in ultrapure water to remove DMAC. Eventually, the Mn-based spheres and Al-based spheres were separately eluted in 0.5 mol/L HCl solution and deionized water for 5 h to eliminate the template Li^+ ion and to obtain the granular adsorbent.

2.4. Experimental set-up

The lithium recycling system consisted of a pretreatment system and a fixed bed adsorption stage, as depicted in Fig. 1. All the tests were conducted under ambient temperature of roughly 25 ºC. The raw raffinate of spent lithium-ion battery was pretreated by coagulation, biochar aerogel adsorption, and ultrafiltration (UF), in sequence. A commercial PACl coagulant with concentrations of 500, 1000, 1200, 1500, 2000 mg/L was tested to determine the optimum dosage. All the coagulation tests were operated in a programmable jar test apparatus (ZR4-6, Zhongrun Water Industry Technology Development Co., Ltd, China). The tests involved fast stirring at 200 rpm for 2 min, followed by slow stirring at 40 rpm for 20 min and static precipitation for 30 min. The obtained supernatant liquid was collected for the subsequent tests. The biochar aerogel was synthesized according to the protocol described in our previous works [37,38]. The biochar aerogel adsorption process was conducted in a shaker at 150 rpm for 2 h with the goal to remove additional organic matter on the clarified supernatant from the previous coagulation step. Subsequently, the solution was pumped into the ultrafiltration device to eliminate turbidity and further organic pollutant. The UF

177 treatment was performed in a cross-flow equipment at a constant pressure of 1.0 bar
178 with an effective membrane area of 17.6 cm^2. The UF process consisted of eight cycles,
179 each cycle including 1 h filtration and 5 min back washing with ultrapure water.

180 The lithium recovery procedure was conducted in a fixed bed column. Considering
181 the concentration of Li^+ ion in the SLR and the adsorption capacity of the adopted
182 adsorbent based on previous studies [39], the volume ratio between adsorbent granules
183 and SLR was set to 1:1.5. To prepare the fixed bed for adsorption, 10 mL of Mn or Al-
184 based granules were placed in an adsorption column, while 15 mL of pretreated SLR
185 was put into a beaker as a feed solution to the column. Adsorption was conducted in a
186 closed-loop system, with the pretreated SLR circulating between the adsorption column
187 and the beaker for 5 h. Adsorption kinetic behaviors were explored by pseudo-first and
188 second-order models. The amount of adsorbed lithium at various times was computed
189 with Eq. (1):

$$q_t = \frac{(C_0 - C_t)V}{m} \tag{1}$$

190 where C_0, m, and V represent the initial lithium concentration, the mass of the adsorbent
191 granules, and the solution volume, respectively. q_t and C_t stand for the adsorbed lithium
192 amount and the Li^+ concentration in the solution at time t.

193 Adsorption selectivity of lithium with respect to other interfering metal ions was
194 assessed by determining the partition coefficient (K_d), the concentration factor (CF),
195 and the separation factor (α_{Me}^{Li}), calculated with the following Eqs. (2-4):

$$K_d = \frac{C_0 - C_e}{C_e} \times \frac{V}{m} \tag{2}$$

$$CF = \frac{q_e(Me)}{C_0(Me)} \tag{3}$$

$$\alpha_{Me}^{Li} = \frac{K_d(Li)}{K_d(Me)} \tag{4}$$

The reusability of adsorbent granules was assessed by adsorption-desorption cycles, including adsorption, desorption, and ultrapure water washing steps. Specifically, the desorption process was carried out in the same way of the adsorption step described above, but with a solution consisting of 0.5 mol/L HCl for Mn-based adsorbent and ultrapure water for Al-based adsorbent, which recirculated between a beaker and the column for 5 h.

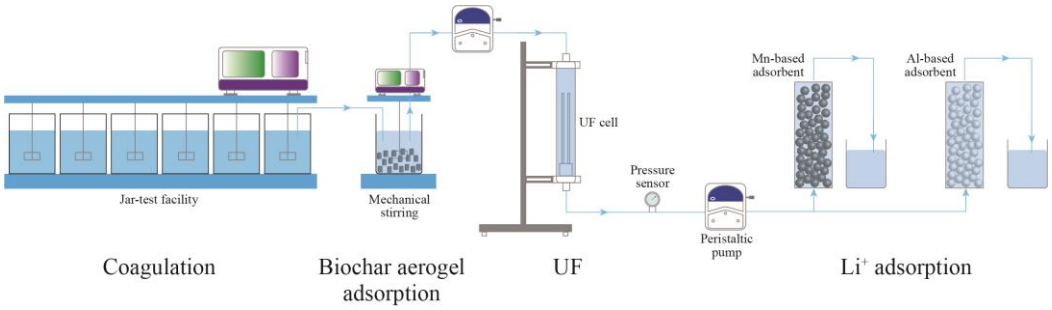

Fig. 1: Schematic flow diagram of the lithium recovery system comprising pretreatment and adsorption steps.

2.5. Analytical methods

Dissolved organic carbon (DOC), UV_{254}, and zeta potential of raw solution and coagulation supernatant under various coagulant dosage were measured with a TOC analyzer (TOC-L, Shimadzu, Japan), UV spectrophotometer (Orion AquaMate 8000, Thermo Fisher, USA), and Zeta-size nano instrument (Nano-ZS90, Malvern, UK), respectively. The three-dimensional excitation-emission matrix fluorescence spectra of

the raw SLR and the solutions obtained after each treatment step were analyzed with a fluorescence spectrophotometer (F7100, Hitachi, Japan). The ion concentration in solution was measured with an atomic absorption spectrometer (AAS, PinAAcle 900T, PerkinElmer, USA) and with ion chromatography (Dionex Integrion HPLC, Thermo Fisher, USA).

The crystalline structure of two types of adsorbent powders, their morphologies, and the elemental distribution of granules were characterized with X-ray diffraction (XRD, DX2700, China) and field emission scanning electron microscopy (FE-SEM, Hitachi, Japan). Nitrogen adsorption-desorption isotherms were obtained with an ASAP 2460 analyzer (Micromeritics, USA) under liquid N_2 atmosphere (77 K). The specific surface area and pore size distribution of the granules were determined applying the Brunaue-Emmett-Teller equation and the Barrett-Joyner-Halenda (BJH) method, respectively.

3. Results and discussion

3.1. Performance of SLR pretreatment and solution characteristics

The characteristics of raw SLR solution are summarized in Table 1. Effects of PACl concentration on the TOC, UV_{254}, and zeta potential of the SLR solution are instead presented in Fig. 2. When PACl dosage increased from 0 to 1500 ppm, TOC and UV_{254} values drastically decreased from 760.5 mg/L to 204.3 mg/L, and from 0.023 cm^{-1} to 0.009 cm^{-1}, respectively. When PACl content further increased to 2000 ppm, TOC and UV_{254} values diminished only slightly to 194.8 mg/L and 0.007 cm^{-1}. Therefore, the optimum PACl dosage was determined to be 1500 ppm. The addition of

PACl decreased the absolute value of the zeta potential, which increased from –10.9 mV (raw SLR) to –3.4 mV (PACl content of 1500 ppm) at the unadjusted pH equal to . A higher PACl concentration likely resulted in more hydroxide precipitation from the suspension [40]. Overall, PACl had remarkable performance on organic matter removal, removing up to 73% of organic matter and representing a suitable choice for SLR coagulation due to the availability and low cost of the coagulant.

Table 1: Characteristics of raw spent lithium-ion battery raffinate.

Parameter	Li (mg/L)	Na (mg/L)	K (mg/L)	Ca (mg/L)	Mg (mg/L)	TOC (mg/L)	UV_{254} (cm^{-1})	TDS (mg/L)	pH
Values	11,470	31,210	126.4	54.56	57.50	769	0.023	112,000	5.54

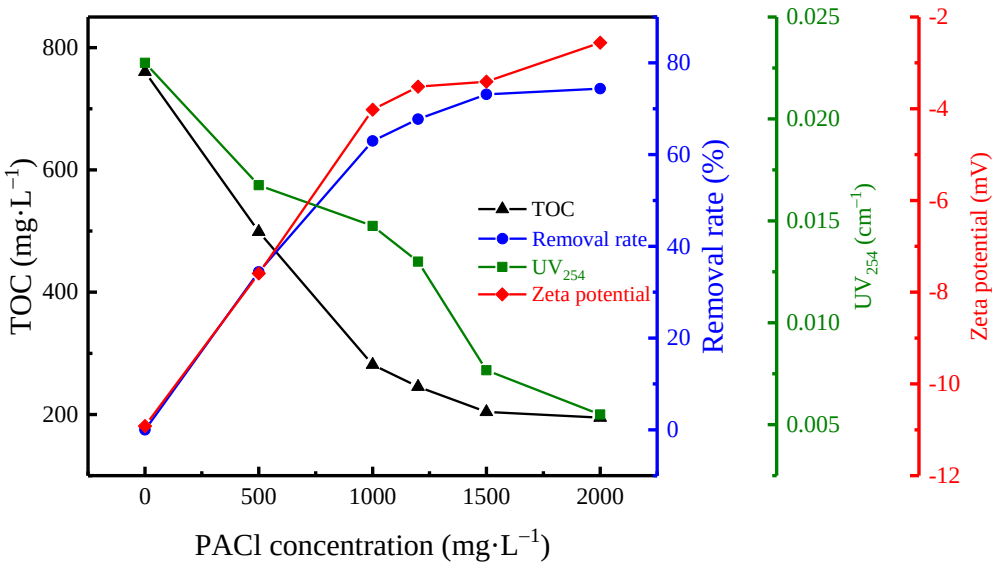

Fig. 2: Variation of TOC, UV_{254}, and zeta potential of the SLR solution with the increased dosage of PACl coagulant. Lines connecting the data points are only a guide for the eye.

Upon clarification, the supernatant was further treated with biochar aerogels and

249 UF membranes. The influence of coagulation and biochar aerogel adsorption processes
250 on UF membrane performance is presented in Fig. 3a. The use of raw SLR as feed
251 solution caused the severest UF membrane fouling, with the membrane flux declining
252 severely to 45.6% of the initial flux, and then recovering to 61.7% of the initial flux at
253 the end of the first cycle of filtration and backwashing. After 8 cycles, the observed flux
254 was only 33.9% of that measured with a pristine membrane, due to the high TOC value
255 of the raw SLR solution and the suspended materials blocking the membrane pores,
256 which was verified with SEM imaging, as shown in Fig. S2. The coagulation treatment
257 somewhat alleviated the UF membrane fouling. In particular, the membrane flux
258 decreased by roughly half in the first filtration cycle, and recovered to 62.5% of the
259 initial flux after backwashing. In this case, the flux decline was mainly attributed to
260 scaling and inorganic components depositing on the UF membrane surface (see Fig.
261 S2). The additional aerogel adsorption treatment further reduced membrane fouling. At
262 the end of first cycle, the flux declined to 63.3% of the initial flux and, after
263 backwashing, the flux recovered to 76.0% of the initial value. At the end of the eighth
264 cycle of filtration, the flux was approximately 55% of the flux measured with a pristine
265 membrane.

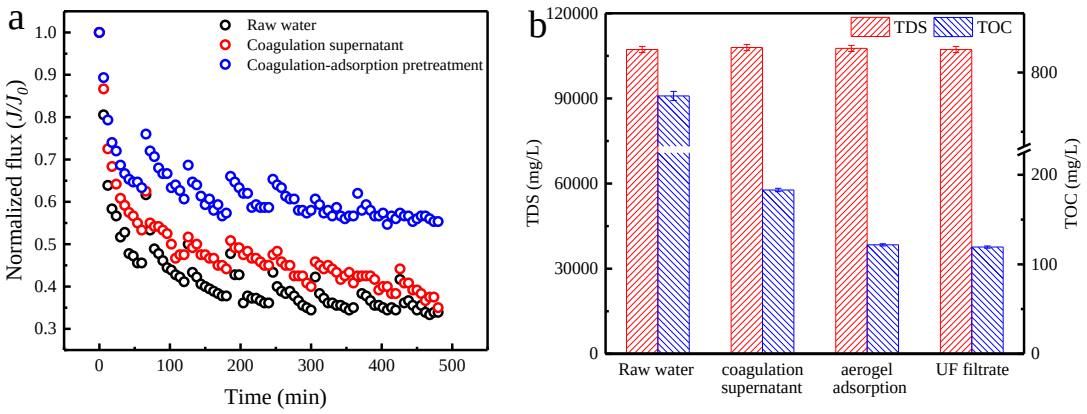

Fig. 3: (a) UF membrane performance for raw and pretreated raffinate of spent lithium-ion battery, and (b) related TDS, TOC variations.

As shown in Fig. 3b, the TOC decreased to 121.8 mg/L and 119.3 mg/L after aerogel adsorption and UF filtration, respectively. Throughout the various pretreatment processes, the TDS concentration remained constant; see Fig. 3b. The evolution of organic matter in the SLR solution was further investigated with three-dimensional fluorescence. Excitation-emission (EEM) spectra of raw SLR and the product stream from every processing stage are reported in Fig. 4(a-d), with the spectra divided into five regions based on previous research analyses [41]. One main peak of emission intensity was observed in all solution samples, centered between region IV and region V, which are related to soluble microbial byproducts and humic-like substance, respectively. The fluorescence regional integration (FRI) analysis indicated that DOM was mainly composed by soluble microbial byproducts (33.7%) and humic-like substances (63.2%); see Fig. 4e. Note that the organic matter composition may be altered in previous processing steps, including the organic extraction agent used for the recovery of rare earth metals from the spent lithium-ion battery.

The raw SLR solution had the highest fluorescence intensity. Upon treatment through PACl coagulant and biochar aerogel adsorption, the peak intensity declined sharply, and then it decreased slightly upon UF filtration. This result is consistent with the TOC removal efficiency reported in Fig. 3b and with the trends in FRI values, which suggest especially high removal of humic-like substances. Indeed, the biochar aerogel typically exhibits a high affinity with humic-like matters, promoting their removal through hydrogen bonding and hydrophobic interaction.

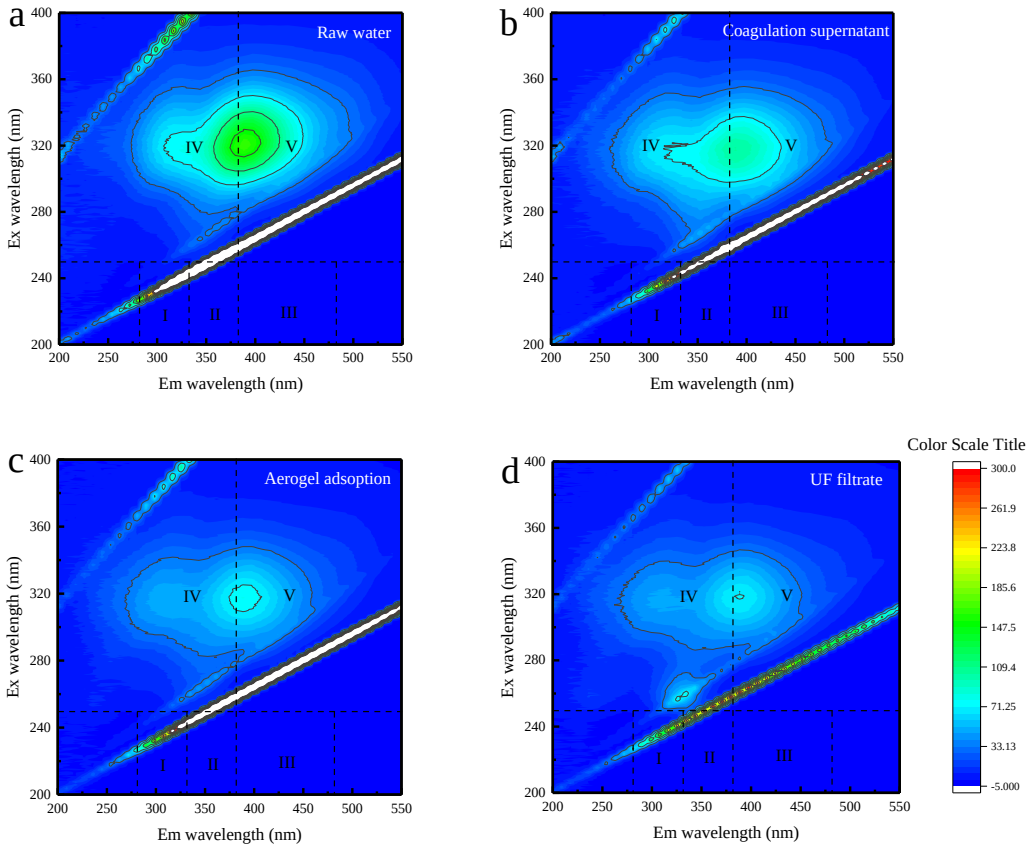

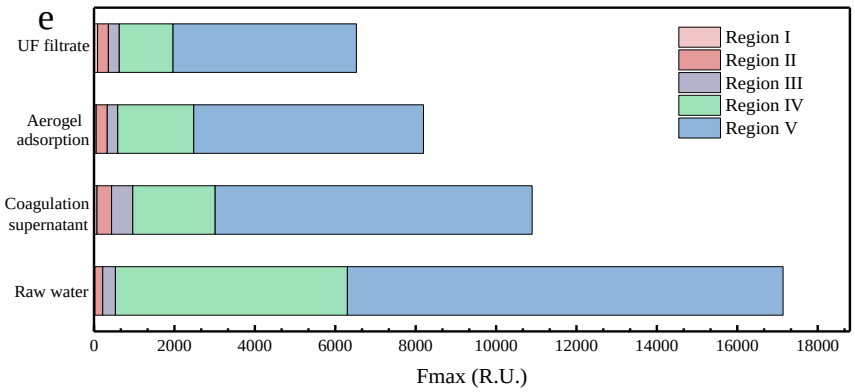

Fig. 4: Three-dimensional excitation-emission (EEM) fluorescence spectra of all SLR samples: (a) raw water, (b) supernatant from the coagulation step, (c) solution upon biochar aerogel adsorption, and (d) UF filtrate. (e) F_{max} of EEM spectra obtained with fluorescence regional integration analysis.

3.2.Characteristics of the Mn and Al-based adsorbents

Fig. 5a and 5e present representative XRD patterns and SEM micrographs of the two kinds of adsorbent precursor powders. The Mn-based powder showed nearly the same diffraction peaks of the standard XRD pattern (PDF No. 46-0810), with main peaks at 2θ = 18.8°, 36.5°, 44.4°, and 64.5°. The spinel structure of the adsorbent observed in the SEM analysis was similar with that described by previous research reports [36]. Both XRD and SEM results suggest the successful synthesis of the Mn-based adsorbent. The XRD pattern of Al-based adsorbent powder was also consistent with the diffraction peaks of the standard pattern (PDF No. 31-0700), with main peaks at 2θ = 11.4°, 23.2°, 40.5°, and 63.2°. The SEM analysis of the Al-based adsorbent suggested a lamellar structure, a layered crystal formed by superposition of octahedral layers of oxygen coordination, indicating the one step coprecipitation method

307 successfully synthesized the Al-based adsorbent.

308 Analyzing the granules produced by combining the precursor powders with PVC,
309 SEM cross-sectional micrographs presented in Fig. 5b and 5f suggest that both
310 adsorbent granules had a partly hollow and highly porous interior structure, with
311 micropores on the surface. The EDS mapping results indicate that Mn and Al were
312 finely distributed, suggesting that the adsorbent powders were uniformly incorporated
313 within the PVC skeleton. Nitrogen adsorption-desorption isotherms of both granule
314 adsorbents, presented in Fig. 5c and 5g, indicate that the adsorbents had mesopores,
315 because of the IV isotherm with an H3 hysteresis loop. The amount of adsorbed N_2 was
316 68.5 cm^3/g and 112.6 cm^3/g for the Mn and for the Al-based adsorbent, respectively.
317 The larger N_2 adsorption was attributed to the relative loose structure of layered Al-
318 based crystal compared to the spinel structure of the Mn-based adsorbent, as observed
319 with SEM analysis. The inset graphs in Fig. 5c and 5g display the pore size distribution
320 according to the BJH method. Mn-based adsorbent had bimodal mesoporous structure
321 distribution with a minor peak corresponding to a small portion of mesopores and a
322 major peak related to the main mesopores. Its mean pore size ranged from 21 to 24 nm.
323 In contrast, the Al-based adsorbent displayed a unimodal mesoporous structure
324 distribution with an average pore size in the range 15-18 nm. Based on BET surface
325 area plot (Fig. 5d and 5h), the Mn-based adsorbent possessed a BET surface area of
326 20.3 m^2/g and a total volume of 0.106 cm^3/g, while the corresponding values for the Al-
327 based adsorbent were 36.6 m^2/g and 0.174 cm^3/g, respectively. Overall, the structure,
328 surface area, and pore characteristics of the materials were highly suitable to achieve

329 potentially high Li adsorption capacity and kinetics, which are the topic discussed in

330 the following chapters.

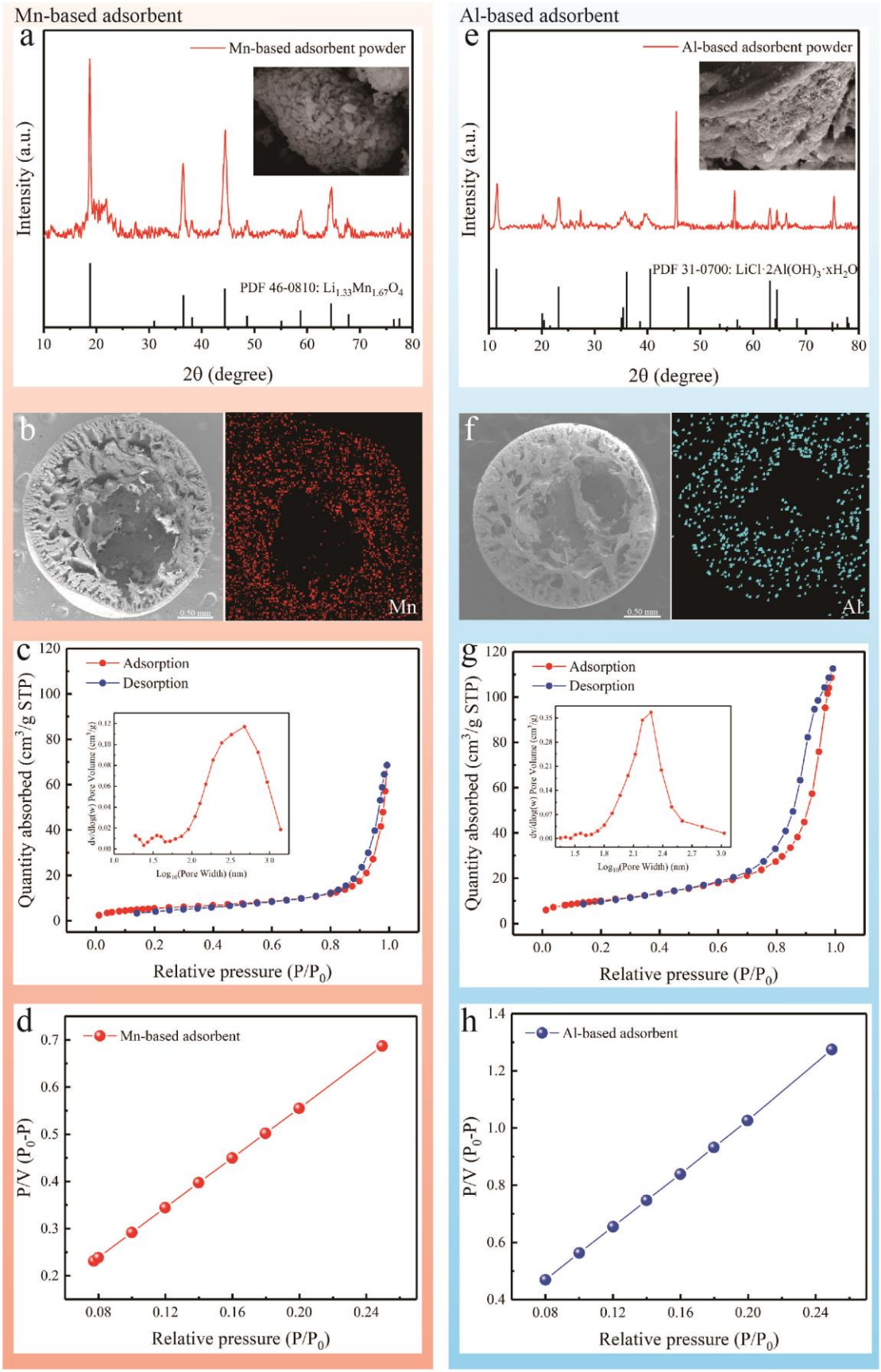

Fig. 5: Mn and Al-based adsorbent properties: (a, e) XRD patterns of the precursor

powders; (b, f) representative SEM micrographs and EDS mapping of the granules obtained by combining the adsorbent powders with PVC; (c, g) N_2 adsorption-desorption curves and resulting pore size distribution of the granules; (d, h) BET surface area plot.

3.3. Adsorption kinetics

The lithium adsorption behavior of both Mn and Al-based adsorbent granules was investigated through adsorption kinetics. The data were fitted to the pseudo-first and second-order kinetic models and the results are displayed in Fig. 6. Both adsorbent granules displayed a rapid lithium adsorption from the SLR solution within the first 1 h, followed by a substantial decrease in the adsorption rate until steady state was reached after roughly 2 h. A relatively rapid adsorption rate observed in this work compared with other previous research [42] may be partly attributed to the higher TDS concentration of SLR (112.3 g/L). The osmosis pressure gradient generated by the salinity difference between SLR solution and the adsorbent spheres may act as a driving force that promotes the transfer of lithium ion from the aqueous phase to solid phase. Fitted kinetic parameters summarized in Table 2 suggest that the differences in R^2 values between pseudo-first-order kinetic model and pseudo-second-order kinetic model were negligible. Therefore, the adsorption process was likely governed by a combination of physical sorption and chemical sorption. According to previous studies, the adsorption kinetics of Mn and Al-based adsorbents are mainly controlled by chemical adsorption [31,36]. Some physical adsorption may possibly be attributed to

355 the interaction of lithium with the PVC skeleton, with ions sorbing onto the surface or

356 the inner pore structure of the adsorbent granules.

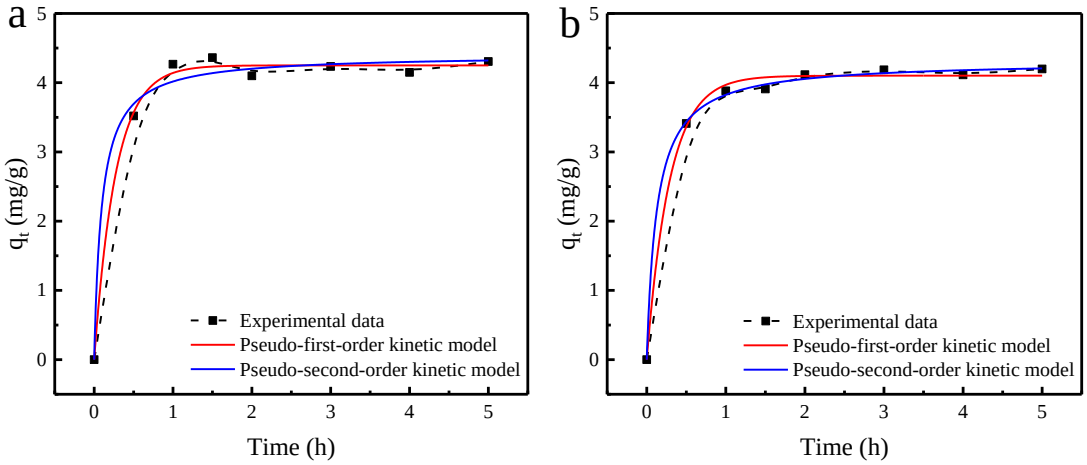

357 Fig. 6: Results of lithium adsorption kinetics test onto (a) Mn-based adsorbent and (b)

358 Al-based adsorbent. Data points were fitted using pseudo-first and pseudo-second

359 order kinetics, with fitting results represented by a red and a blue line, respectively.

360

361 Table 2: Results of fitting the lithium adsorption kinetics data with pseudo-first-order

362 and pseudo-second-order models.

	Pseudo-first-model $q_{e,cal}$ (mg/g)	k_1 (min^{-1})	R^2	Pseudo-second-model $q_{e,cal}$ (mg/g)	K_2 ($g \cdot min^{-1}h^{-1}$)	R^2
Mn-based	4.25	3.66	0.9947	4.40	2.36	0.9867
Al-based	4.10	3.43	0.9955	4.31	1.81	0.9984

363

364 3.4. Performance of the integrated multiple stage adsorption process

365 An integrated three-stage adsorption process was designed and evaluated to

366 maximize the recovery of lithium from SLR. Results presented in Fig. 7 imply that the

367 adsorption on both adsorbent granules decreased in subsequent adsorption stages, likely

368 due to the reduced concentration gradient. At the end of three-stage adsorption, the

concentration of Li^+ ion decreased from 1147 mg/L to approximately 373 mg/L and 420 mg/L for Mn and Al-based adsorbent, respectively, and the recovery rate reached values of 67.5% and 63.4%. The Mn-based adsorbent displayed a relatively superior recovery performance, attributed to specific recognition of Li^+ ions by ion exchange of Li^+/H^+, which is possibly a more suitable mechanism compared to the intercalation phenomena characterizing the main adsorption mechanism of the Al-based adsorbent. However, overall, both adsorbents had a desirable performance for lithium recycling from raffinate of spent lithium-ion battery.

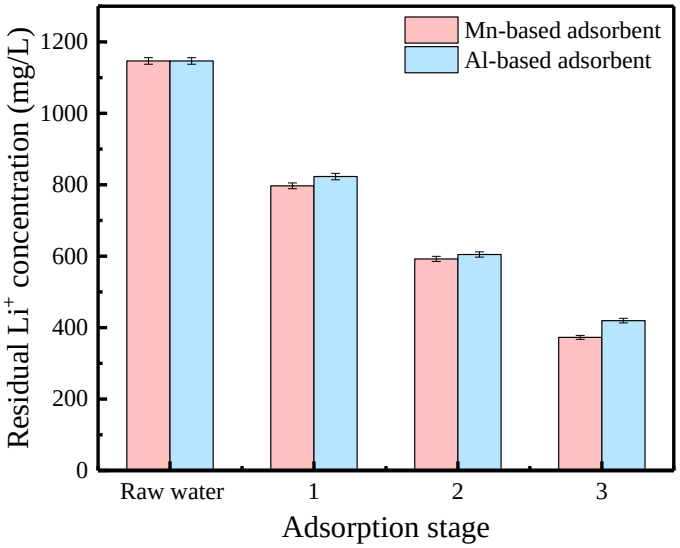

Fig. 7. Multi-stage adsorption performance of Mn and Al-based adsorbent granules.

3.5. Selectivity performance

It is important to assess the selectivity of both Mn and Al-based adsorbents for lithium ion in the presence of interfering ions (Na^+, K^+, Ca^{2+}, Mg^{2+}) in the SLR, especially the Na^+ ion characterized by high concentrations up to roughly 31200 mg/L. Fig. 8 presents the partition coefficients (K_d), while other adsorption and selectivity

parameters are summarized in Table 3 and Table 4. The lithium partition coefficients associated with both adsorbents were larger than those of other ions, particularly Na^+. Specifically, the K_d value characterizing the Mn-based adsorbent (6.62 mL/g) was greater than that determined for the Al-based adsorbent (4.05 mL/g), consistent with adsorption capacity results presented above. Compared with the layered crystal structure of Al-based adsorbent, the relatively higher selective separation of Mn-based adsorbent to lithium may be attributed to its spinel structure providing an ionic sieve effect that promotes preferential adsorption of ions with radius similar to that of the adsorption sites. It should be noted that the adsorption capacity for both adsorbents to Na^+ was also large, which may be explained by the following reasons. On the one hand, the concentration of Na^+ ion in SLR was 27.2 times higher than the Li^+ concentration, which may promote much more substantial physical adsorption onto the surface and inner cavity of the PVC skeleton. This hypothesis was corroborated by the EDS mapping determined on granule adsorbent after they were used for adsorption; see Fig. S3. On the other hand, although the selectivity for Li^+ with respect to Na^+ was high for both adsorbent materials, a proportion of adsorption sites were indeed consumed by Na^+, which is an unavoidable phenomenon because of the concentration ratios in the SLR solution. That being said, the combination of capacity and selectivity results suggests the suitability of both adsorbent for lithium uptake from SLR, with a slight preference for Mn-based materials, possibly due to their more appropriate structural characteristics.

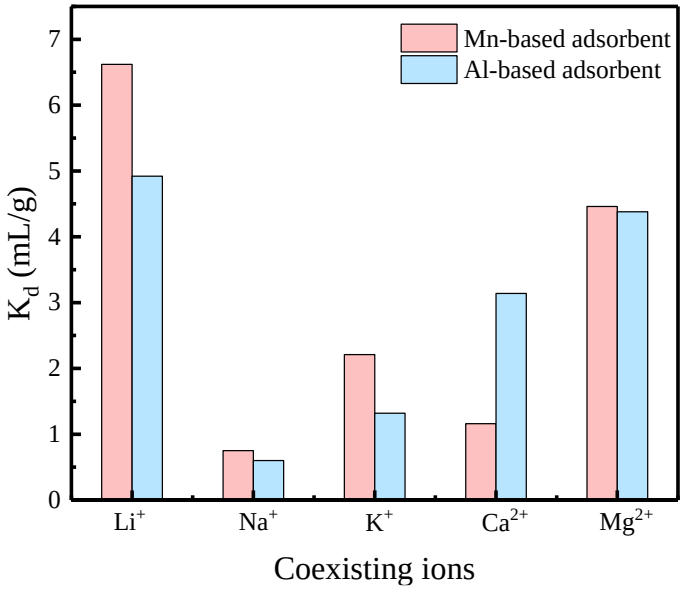

406

407 Fig. 8. Partition coefficients (K_d) determined for both adsorbent granules for

408 coexisting cations.

409

410 Table 3: Adsorption selectivity of Mn-based adsorbent from SLR.

	C_0 (mg/L)	C_e (mg/L)	q_e (mg/g)	K_d (mL/g)	CF (mL/g)	α_{Me}^{Li}
Li^+	1,147	750	4.96	6.62	4.33	1
Na^+	31,200	29,400	22.2	0.75	0.71	8.79
K^+	126	107	0.24	2.21	1.88	3.00
Ca^{2+}	54.6	49.9	0.06	1.16	1.06	4.09
Mg^{2+}	57.5	42.4	0.19	4.46	3.29	1.49

411

412

413

414

415

Table 4: Adsorption selectivity of Al-based adsorbent from SLR.

	C_0 (mg/L)	C_e (mg/L)	q_e (mg/g)	K_d (mL/g)	CF (mL/g)	α_{Me}^{Li}
Li^+	1,147	823	4.05	4.92	3.53	1
Na^+	31,200	29,800	17.9	0.60	0.57	8.17
K^+	126	114	0.15	1.32	1.20	3.71
Ca^{2+}	54.6	43.6	0.14	3.14	2.51	1.41
Mg^{2+}	57.5	42.6	0.18	4.38	3.24	1.12

3.6. Reusability and stability of Mn and Al-based adsorbents

The reusability of both adsorbent granules was evaluated in twenty cycles of adsorption and desorption. The lithium adsorption/desorption capacity assessed in every cycle is presented in Fig. 9. The adsorbents exhibited relatively stable performance, with adsorption capacities fluctuating around 4 mg/g for Mn-based adsorbent and 3.5 mg/g for Al-based adsorbent across the cycles. Concurrently, both adsorbents showed stable desorption behavior, with desorption capacities fluctuating around 3.5 mg/g and 2.8 mg/g for Mn-based granules and Al-based granules, respectively. For Mn-based granules, the seemingly inconsistent value of lithium desorption compared to that of previous adsorption in the first cycle may be explained with the incomplete washing out of adsorbent precursor from the synthesized material, resulting in some template Li^+ still occupying the binding sites during the first cycle of adsorption, then washed out during the subsequent desorption step.

Fig. 9a presents results obtained in the investigation of the adsorbent stability. Mn loss from Mn-based materials was 0.45% after the first cycle, and it decreased to around

0.2% for the following cycles. A higher Mn loss in the first cycle is likely ascribed to the incompletely fixed Mn element in the adsorbent crystal structure during the sintering procedure, with a portion of the element that was only attached to the surface of the powdered adsorbent, thus easily eluted once in contact with the desorption solution. The results presented in Fig. 9b suggest that during the 20 cycles, the Al-based granule suffered instead negligible Al loss, namely, less than 0.06‰. A relatively larger Mn loss during all cycles may be attributed to the effect of acid treatment, which would likely induce electron transfer from trivalent manganese in the crystal structure to tetravalent manganese in the surface. After obtaining sufficient electrons, tetravalent manganese would convert to bivalent manganese, in turn subject to dissolution [43]. Overall, the remarkable stability of both adsorbents imply the potential for long-term application of both adsorbents for lithium selective adsorption recovery.

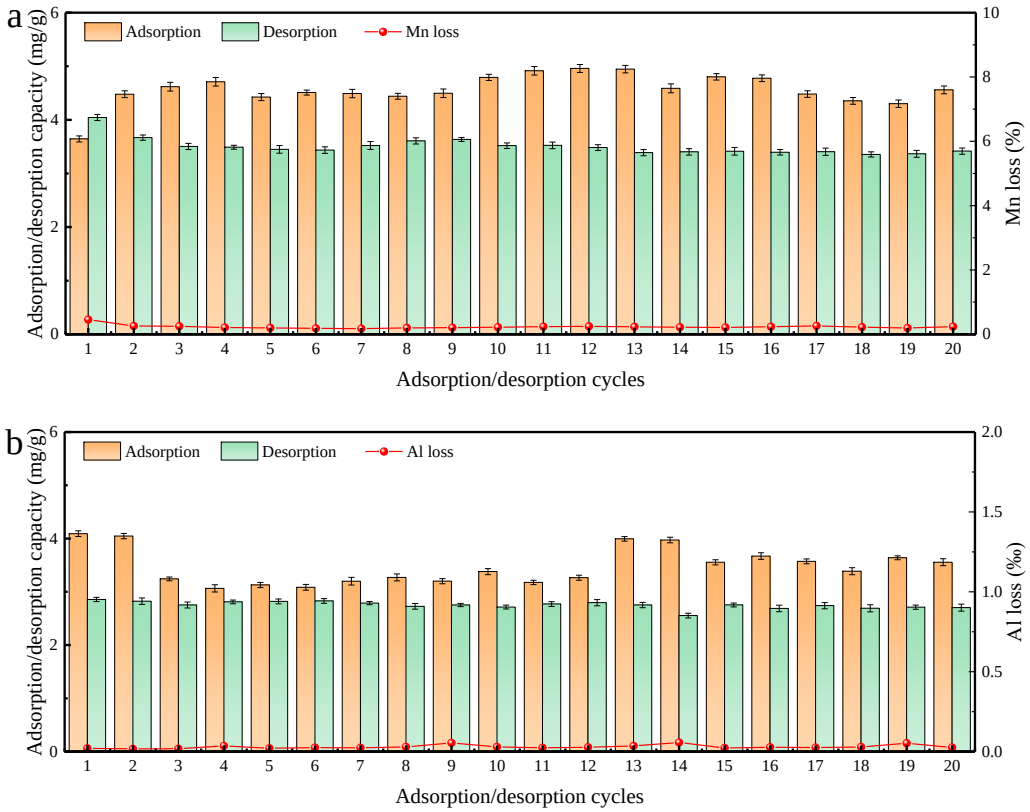

Fig. 9: Adsorption-desorption capacity of Li^+ and related Mn, Al loss in different, subsequent cycles of adsorption and desorption: (a) Mn-based adsorbent granules, (b) Al-based adsorbent granules.

4. Conclusion

This paper discussed materials and their application in an integrated approach for lithium recovery from spent lithium-ion battery raffinate (SLR), combining pretreatment of the solution via PACl coagulation, biochar aerogel adsorption, and ultrafiltration, with lithium adsorption onto Mn and Al-based adsorbent granules. The pretreatment steps effectively removed organic constituents of the SLR, which decreased from roughly 761 mg/L to 119 mg/L without observable lithium-ion loss. Both Mn and Al-based adsorbent granules exhibited rapid adsorption of lithium from the pretreated SLR, reaching saturation within 2 h, with final capacity in the range 4-5 mg of lithium per g of adsorbent granular material. Notably, the partition coefficients of Li^+ for Mn-based (6.62 mL/g) and Al-based (4.92 mL/g) adsorbents were significantly higher than those of other ions, particularly Na^+ (0.75 mL/g for Mn-based adsorbent and 0.60 mL/g for Al-based adsorbent), suggesting effective separation of Li^+ and Na^+. The Mn-based adsorbent showed superior adsorption capacity compared to Al-based adsorbent, attributed to its favorable structure. Both adsorbents also presented remarkable reusability. After twenty adsorption/desorption cycles, the adsorption capacities of Mn and Al-based adsorbents reached a stable behavior, maintaining values of 4.5 mg/g and 3.5 mg/g, respectively, which was only about 10-

15% lower than the values measured for the as-synthesized materials in their first cycle of application. While the Mn-based adsorbent provided a better adsorption capacity, it experienced a relatively higher element loss, equal to approximately 0.2% Mn loss per cycle. On the contrary, Al loss was negligible from Al-based materials. This study indicates the effectiveness of pretreatment followed by Mn and Al-based adsorbent adsorption as a promising and technically feasible strategy for lithium recovery from SLR.

Notes

The authors declare no competing financial interests.

Acknowledgement:

This work was supported by the National Natural Science Foundation of China (52270075, 52070134), Cultivation Program for Young and Middle-aged Leading Talents in Science and Technology (2023SCU17), Sichuan University and Zigong City People's Government Strategic Cooperation Project (2022CDZG-7), and Sichuan University and Yibin City People's Government Strategic Cooperation Project (2020CDYB-2). A.T. acknowledges the support from the MICS (Made in Italy – Circular and Sustainable) Extended Partnership and from the European Union NextGenerationEU (National Recovery and Resilience Plan (NRRP) – Mission 4, Component 2, Investment 1.3 – D.D. 1551.11-10-2022, PE00000004). This manuscript reflects only the authors' views and opinions, and the funding agencies cannot be

considered responsible for them.

References:

[1] Z. Sun, H. Cao, Y. Xiao, J. Sietsma, W. Jin, H. Agterhuis, Y. Yang, Toward Sustainability for Recovery of Critical Metals from Electronic Waste: The Hydrochemistry Processes, ACS Sustainable Chem. Eng. 5 (2017) 21–40. https://doi.org/10.1021/acssuschemeng.6b00841.

[2] B. Swain, Recovery and recycling of lithium: A review, Separation and Purification Technology 172 (2017) 388–403. https://doi.org/10.1016/j.seppur.2016.08.031.

[3] P.K. Choubey, M. Kim, R.R. Srivastava, J. Lee, J.-Y. Lee, Advance review on the exploitation of the prominent energy-storage element: Lithium. Part I: From mineral and brine resources, Minerals Engineering 89 (2016) 119–137. https://doi.org/10.1016/j.mineng.2016.01.010.

[4] X. Li, Y. Mo, W. Qing, S. Shao, C.Y. Tang, J. Li, Membrane-based technologies for lithium recovery from water lithium resources: A review, Journal of Membrane Science 591 (2019) 117317. https://doi.org/10.1016/j.memsci.2019.117317.

[5] T. Raj, K. Chandrasekhar, A.N. Kumar, P. Sharma, A. Pandey, M. Jang, B.-H. Jeon, S. Varjani, S.-H. Kim, Recycling of cathode material from spent lithium-ion batteries: Challenges and future perspectives, Journal of Hazardous Materials 429 (2022) 128312. https://doi.org/10.1016/j.jhazmat.2022.128312.

[6] J. Xiao, J. Li, Z. Xu, Novel Approach for in Situ Recovery of Lithium Carbonate from Spent Lithium Ion Batteries Using Vacuum Metallurgy, Environ. Sci. Technol. 51 (2017) 11960–11966. https://doi.org/10.1021/acs.est.7b02561.

[7] I.-Y.L. Hsieh, M.S. Pan, W.H. Green, Transition to electric vehicles in China: Implications for private motorization rate and battery market, Energy Policy 144 (2020) 111654. https://doi.org/10.1016/j.enpol.2020.111654.

[8] S. Gao, W. Liu, D. Fu, X. Liu, Research progress on recovering the components of spent Li-ion batteries, New Carbon Materials 37 (2022) 435–460. https://doi.org/10.1016/S1872-5805(22)60605-X.

[9] R. Xu, S. Lei, T. Wang, C. Yi, W. Sun, Y. Yang, Lithium recovery and solvent reuse from electrolyte of spent lithium-ion battery, Waste Management 167 (2023) 135–140. https://doi.org/10.1016/j.wasman.2023.05.034.

[10] X. Zhu, Y. Li, M. Gong, R. Mo, S. Luo, X. Yan, S. Yang, Recycling Valuable Metals from Spent Lithium-Ion Batteries Using Carbothermal Shock Method, Angew Chem Int Ed 62 (2023) e202300074. https://doi.org/10.1002/anie.202300074.

[11] E. Yoo, U. Lee, J.C. Kelly, M. Wang, Life-cycle analysis of battery metal recycling with lithium recovery from a spent lithium-ion battery, Resources, Conservation and Recycling 196 (2023) 107040. https://doi.org/10.1016/j.resconrec.2023.107040.

[12] M. He, P. Zhang, X. Duan, L. Teng, H. Li, F. Meng, Q. Liu, W. Liu, Selective recovery of lithium from spent lithium-ion battery by an emission-free sulfation roasting strategy, Process Safety and Environmental Protection 177 (2023) 1035–1044. https://doi.org/10.1016/j.psep.2023.07.065.

[13] C. Liu, J. Lin, H. Cao, Y. Zhang, Z. Sun, Recycling of spent lithium-ion batteries

in view of lithium recovery: A critical review, Journal of Cleaner Production 228 (2019) 801–813. https://doi.org/10.1016/j.jclepro.2019.04.304.
[14] J. Xiao, J. Li, Z. Xu, Challenges to Future Development of Spent Lithium Ion Batteries Recovery from Environmental and Technological Perspectives, Environ. Sci. Technol. 54 (2020) 9–25. https://doi.org/10.1021/acs.est.9b03725.
[15] X. Hu, E. Mousa, G. Ye, Recovery of Co, Ni, Mn, and Li from Li-ion batteries by smelting reduction - Part II: A pilot-scale demonstration, Journal of Power Sources 483 (2021) 229089. https://doi.org/10.1016/j.jpowsour.2020.229089.
[16] J. Xu, Y. Jin, K. Liu, N. Lyu, Z. Zhang, B. Sun, Q. Jin, H. Lu, H. Tian, X. Guo, D. Shanmukaraj, H. Wu, M. Li, M. Armand, G. Wang, A green and sustainable strategy toward lithium resources recycling from spent batteries, Sci. Adv. 8 (2022) eabq7948. https://doi.org/10.1126/sciadv.abq7948.
[17] C. Yi, P. Ge, X. Wu, W. Sun, Y. Yang, Tailoring carbon chains for repairing graphite from spent lithium-ion battery toward closed-circuit recycling, Journal of Energy Chemistry 72 (2022) 97–107. https://doi.org/10.1016/j.jechem.2022.05.002.
[18] J. Xiao, B. Niu, Z. Xu, Highly efficient selective recovery of lithium from spent lithium-ion batteries by thermal reduction with cheap ammonia reagent, Journal of Hazardous Materials 418 (2021) 126319. https://doi.org/10.1016/j.jhazmat.2021.126319.
[19] E. Gerold, F. Kadisch, R. Lerchbammer, H. Antrekowitsch, Bio-metallurgical recovery of lithium, cobalt, and nickel from spent NMC lithium ion batteries: A comparative analysis of organic acid systems, Journal of Hazardous Materials Advances 13 (2024) 100397. https://doi.org/10.1016/j.hazadv.2023.100397.
[20] L. Yang, Z. Gao, T. Liu, M. Huang, G. Liu, Y. Feng, P. Shao, X. Luo, Direct Electrochemical Leaching Method for High-Purity Lithium Recovery from Spent Lithium Batteries, Environ. Sci. Technol. 57 (2023) 4591–4597. https://doi.org/10.1021/acs.est.3c00287.
[21] L.F. Guimarães, A.B. Botelho Junior, D.C.R. Espinosa, Sulfuric acid leaching of metals from waste Li-ion batteries without using reducing agent, Minerals Engineering 183 (2022) 107597. https://doi.org/10.1016/j.mineng.2022.107597.
[22] Y. Kikuchi, A. Heiho, Y. Dou, I. Suwa, I.-C. Chen, Y. Fukushima, C. Tokoro, Defining Requirements on Technology Systems Assessment from Life Cycle Perspectives: Cases on Recycling of Photovoltaic and Secondary Batteries, IJAT 14 (2020) 890–908. https://doi.org/10.20965/ijat.2020.p0890.
[23] Y. Ma, S. Huang, X. Liu, J. Huang, Y. Zhang, K. Li, Z. Zhang, X. Yu, Z. Fu, Lithium enrichment and migration mechanism in the evaporation process of sodium aulphate subtype salt lake brine, Desalination 566 (2023) 116908. https://doi.org/10.1016/j.desal.2023.116908.
[24] R. Coterillo, L.-E. Gallart, E. Fernández-Escalante, J. Junquera, P. García-Fernández, I. Ortiz, R. Ibañez, M.-F. San-Román, Selective extraction of lithium from seawater desalination concentrates: Study of thermodynamic and equilibrium properties using Density Functional Theory (DFT), Desalination 532 (2022) 115704. https://doi.org/10.1016/j.desal.2022.115704.

[25] J. Xu, X. Wei, J. Han, W. Qin, Synthesis and optimisation mechanism of functionalised adsorption materials for lithium-ion extraction from salt water: A review, Separation and Purification Technology 339 (2024) 126237. https://doi.org/10.1016/j.seppur.2023.126237.
[26] S. Xu, J. Song, Q. Bi, Q. Chen, W.-M. Zhang, Z. Qian, L. Zhang, S. Xu, N. Tang, T. He, Extraction of lithium from Chinese salt-lake brines by membranes: Design and practice, Journal of Membrane Science 635 (2021) 119441. https://doi.org/10.1016/j.memsci.2021.119441.
[27] L. Wu, C. Zhang, S. Kim, T.A. Hatton, H. Mo, T.D. Waite, Lithium recovery using electrochemical technologies: Advances and challenges, Water Research 221 (2022) 118822. https://doi.org/10.1016/j.watres.2022.118822.
[28] H. Yu, G. Naidu, C. Zhang, C. Wang, A. Razmjou, D.S. Han, T. He, H. Shon, Metal-based adsorbents for lithium recovery from aqueous resources, Desalination 539 (2022) 115951. https://doi.org/10.1016/j.desal.2022.115951.
[29] W. Qu, Y. Fu, Y. Zhang, W. Wang, C. Xu, C. Liu, Y. Zhang, Q. Wang, B. Liu, Structural/surficial dual regulated granular H_2TiO_3 lithium-ion sieves for lithium extraction from salt lake brine, Journal of Cleaner Production 449 (2024) 141789. https://doi.org/10.1016/j.jclepro.2024.141789.
[30] R. Zhu, S. Wang, C. Srinivasakannan, S. Li, S. Yin, L. Zhang, X. Jiang, G. Zhou, N. Zhang, Lithium extraction from salt lake brines with high magnesium/lithium ratio: a review, Environ Chem Lett 21 (2023) 1611–1626. https://doi.org/10.1007/s10311-023-01571-9.
[31] J. Zhong, S. Lin, J. Yu, Li^+ adsorption performance and mechanism using lithium/aluminum layered double hydroxides in low grade brines, Desalination 505 (2021) 114983. https://doi.org/10.1016/j.desal.2021.114983.
[32] Y. Sun, X. Guo, S. Hu, X. Xiang, Highly efficient extraction of lithium from salt lake brine by LiAl-layered double hydroxides as lithium-ion-selective capturing material, Journal of Energy Chemistry 34 (2019) 80–87. https://doi.org/10.1016/j.jechem.2018.09.022.
[33] N. Xu, S. Li, M. Guo, Z. Qian, W. Li, Z. Liu, Synthesis of $H_4Mn_5O_{12}$ Nanotubes Lithium Ion Sieve and Its Adsorption Properties for Li^+ from Aqueous Solution, ChemistrySelect 4 (2019) 9562–9569. https://doi.org/10.1002/slct.201901764.
[34] Z.-Y. Ji, M.-Y. Zhao, Y.-Y. Zhao, J. Liu, J.-L. Peng, J.-S. Yuan, Lithium extraction process on spinel-type $LiMn_2O_4$ and characterization based on the hydrolysis of sodium persulfate, Solid State Ionics 301 (2017) 116–124. https://doi.org/10.1016/j.ssi.2017.01.018.
[35] L. Tang, S. Huang, Y. Wang, D. Liang, Y. Li, J. Li, Y. Wang, Y. Xie, W. Wang, Highly Efficient, Stable, and Recyclable Hydrogen Manganese Oxide/Cellulose Film for the Extraction of Lithium from Seawater, ACS Appl. Mater. Interfaces 12 (2020) 9775–9781. https://doi.org/10.1021/acsami.9b21612.
[36] L. Tian, Y. Liu, P. Tang, Y. Yang, X. Wang, T. Chen, Y. Bai, A. Tiraferri, B. Liu, Lithium extraction from shale gas flowback and produced water using $H_{1.33}Mn_{1.67}O_4$ adsorbent, Resources, Conservation and Recycling 185 (2022) 106476. https://doi.org/10.1016/j.resconrec.2022.106476.

[37] Y. Liu, P. Tang, Y. Zhu, W. Xie, P. Yang, Z. Zhang, B. Liu, Green aerogel adsorbent for removal of organic compounds in shale gas wastewater: High-performance tuning and adsorption mechanism, Chemical Engineering Journal 416 (2021) 129100. https://doi.org/10.1016/j.cej.2021.129100.
[38] J. Shu, Q. Wu, X. Ren, P. Tang, G. Chen, X. Cheng, C. Chen, A. Tiraferri, B. Liu, Efficiency and Mechanisms of Biochar Aerogel-Assisted Biodegradation of Taste and Odor Compounds in a One-Step Membrane Bioreactor for Rural Drinking Water Production, ACS EST Eng. 4 (2024) 300–309. https://doi.org/10.1021/acsestengg.3c00233.
[39] L. Tian, Y. Yang, G. Chen, A. Tiraferri, B. Liu, Efficient Lithium Extraction from Shale Gas Wastewater Using Sodium Alginate/$H_{1.33}Mn_{1.67}O_4$ Composite Granular Adsorbents, ACS EST Eng. 3 (2023) 1676–1685. https://doi.org/10.1021/acsestengg.3c00167.
[40] H. Chang, B. Liu, B. Yang, X. Yang, C. Guo, Q. He, S. Liang, S. Chen, P. Yang, An integrated coagulation-ultrafiltration-nanofiltration process for internal reuse of shale gas flowback and produced water, Separation and Purification Technology 211 (2019) 310–321. https://doi.org/10.1016/j.seppur.2018.09.081.
[41] P. Tang, B. Liu, Y. Zhang, H. Chang, P. Zhou, M. Feng, V.K. Sharma, Sustainable reuse of shale gas wastewater by pre-ozonation with ultrafiltration-reverse osmosis, Chemical Engineering Journal 392 (2020) 123743. https://doi.org/10.1016/j.cej.2019.123743.
[42] W. Ding, J. Zhang, Y. Liu, Y. Guo, T. Deng, X. Yu, Synthesis of granulated H4Mn5O12/chitosan with improved stability by a novel cross-linking strategy for lithium adsorption from aqueous solutions, Chemical Engineering Journal 426 (2021) 131689. https://doi.org/10.1016/j.cej.2021.131689.
[43] A. Gao, Z. Sun, S. Li, X. Hou, H. Li, Q. Wu, X. Xi, The mechanism of manganese dissolution on $Li_{1.6}Mn_{1.6}O_4$ ion sieves with HCl, Dalton Trans. 47 (2018) 3864–3871. https://doi.org/10.1039/C8DT00033F.